

Chitosan/bovine serum albumin co-micropatterns on functionalized titanium surfaces and their effects on osteoblasts

Dan Li · Xiong Lu · Hong Lin · Fuzeng Ren · Yang Leng

Received: 13 April 2012 / Accepted: 31 October 2012 / Published online: 8 November 2012
© Springer Science+Business Media New York 2012

Abstract Chitosan (CS)/bovine serum albumin (BSA) micropatterns were prepared on functionalized Ti surfaces by micro-transfer molding (μ -TM). μ -TM realized the spatially controlled immobilization of cells and offered a new way of studying the interaction between micropatterns and cells. Two kinds of micropatterns were produced: (1) microgrooves representing a discontinuously grooved co-micropattern, with the rectangular CS region separated by BSA walls; (2) microcylinders representing a continuously interconnected co-micropattern, with the net-like CS region separated by BSA cylinders. A comparison of cell behaviors on the two types of micropatterns indicated that the shape rather than the size had a dominant effect on cell proliferation. The micropattern size in the same range of cell diameters favored cell proliferation. However, cell differentiation was more sensitive to the size rather than to the shape of the micropatterns. In conclusion, cell behavior can be regulated by micropatterns integrating different materials.

1 Introduction

Titanium and its alloys are widely used as orthopedic and dental implant materials because of their good corrosion

resistance, fatigue endurance, and excellent load-bearing ability [1, 2]. Ti is bioinert and has difficulty in forming direct bonds with surrounding bone tissue. Modifying Ti surfaces to promote bone growth has been a research focus in biomedical surface engineering. A large quantity of bioactive molecules, such as peptides [3–5], polyphosphoric acids [6, 7], and proteins [8, 9], have been grafted onto Ti surfaces to promote osteoblast adhesion and bone growth. Other molecules that could be used for Ti surface modification include chitosan (CS) and bovine serum albumin (BSA). CS is a natural polysaccharide with good biocompatibility, antibacterial properties [10], and osteogenic properties [11]. Bumgardner et al. [12, 13] discussed the possibility of CS coatings on Ti for orthopedic and craniofacial/dental implants, and found that CS coatings support the attachment and proliferation of osteoblasts and improve osseointegration. BSA is a large globular protein with numerous biochemical applications and is used as a nutrient in cell culture. BSA can act as a blocking agent to inhibit the non-specific adsorption of other proteins and cells [14, 15].

Micropatterns have long been thought to be potent factors in controlling cell behavior. Recently, a growing number of researchers have investigated cell behavior on well-defined microfabricated surfaces to study quantitatively the topographical effects on cell behavior. denBraber et al. [16] studied rat dermal fibroblast (RDF) behavior on bulk Ti with microgrooves and found that RDFs tend to orient along microgrooves. Chehroudi et al. [17] reported that micro-textured Ti surfaces can induce epithelial downgrowth around implants. Hamilton et al. [18] observed that micropits and micropillars of epoxy resin significantly enhance osteoblast mineralization. Zinger et al. [19] used titanium disks with microcavities as substrates for MG63 osteoblast-like cell culture. They

D. Li · X. Lu (✉) · H. Lin
Key Lab of Advanced Technologies of Materials,
Ministry of Education, School of Materials Science
and Engineering, Southwest Jiaotong University,
Chengdu 610031, Sichuan, China
e-mail: luxiong_2004@163.com

F. Ren · Y. Leng
Department of Mechanical Engineering, Hong Kong University
of Science and Technology, Kowloon, Hong Kong, China

found that 100 μm cavities favor osteoblast growth and attachment, whereas submicron structures within the cavities enhance osteoblast differentiation. Mata et al. [20] reported significantly increased connective tissue progenitor cell proliferation on posts 10 μm in diameter compared with smooth polydimethylsiloxane (PDMS). In summary, the diversity of micropatterns, including microgrooves, pits, and grids, affect the response of cells to surface microgeometry.

Various materials were utilized to prepare micropatterns, such as hyaluronic acid, heparin [21], gelatin [22], collagen, laminin, vitronectin, fibronectin [23], polylactic acid [24], poly lactic-co-glycolic acid [25, 26], CS [27], BSA [28], hydroxylapatite [29], and titanium [30]. The effect of micropatterns on cells is a complex phenomenon. A previous study in our lab showed the synergistic effects of surface topography and material chemistry on cell behavior and revealed that results drawn from one type of material cannot simply be applied to another [30]. Different materials could be integrated into one substrate to form composite micropatterns and study cell behavior.

Modifying Ti surfaces with micropatterns consisting of two or more kinds of bioactive molecules is a promising research direction. Co-micropatterns generally include one cell-adhesive material patterned against another non-adhesive material that can control cell spacing and position. Healy et al. [31] studied bone-derived cell attachment, migration, and mineralization on N-(2-aminoethyl)-3-aminopropyl-trimethoxysilane (EDS)/dimethyldichlorosilane (DMS)-patterned surfaces and revealed different rates of tissue mineralization on EDS and DMS regions. Kam et al. [32] patterned cell-adhesive arrays of N1-[3-(trimethoxysilyl)propyl]diethylenetriamine (DETA) against non-adhesive octadecyltrichlorosilane (OTS). LRM55 astroglial cells can adhere and spread upon single hexagonal DETA arrays, and cell density is correlated with hexagonal DETA width. Singhvi et al. [33] patterned hexadecanethiol [$\text{HS}(\text{CH}_2)_{15}\text{CH}_3$] micro-squares surrounded by a polyethylene glycol-terminated alkanethiol [$\text{HS}(\text{CH}_2)_{11}(\text{OCH}_2\text{CH}_2)_6\text{OH}$]. Hepatocytes maintain normal albumin secretion levels and low growth rate on small squares (40/40 μm). However, they exhibit low albumin secretion levels and high growth rate on un-patterned substrates or large adhesive islands. Clark et al. [34] patterned hydrophobic DMS lines on the adhesive fused quartz substrate and found that cell response is dependent on cell type and substrate surface geometry. Thus, composite micropatterns significantly influence cell behavior.

CS/BSA composite micropatterns can accurately control cell attachment because CS is a cell-adhesive polysaccharide and BSA is a cell-resistant protein. Feng et al. [35] prepared CS/BSA co-micropatterns on an aldehyde-enriched glass substrate by microcontact printing ($\mu\text{-CP}$).

However, the quantity of chemicals introduced by the $\mu\text{-CP}$ method is limited. In addition, the ability of CS/BSA co-micropatterns produced by $\mu\text{-CP}$ to control cell localization and cell growth guidance needs to be further confirmed. In our recent studies, we have demonstrated the possibility of producing CS/BSA composite micropatterns on silicon surfaces by microtransfer molding ($\mu\text{-TM}$) [36]. $\mu\text{-TM}$ is a soft lithography technology for the fabrication of microstructures developed by Whitesides, which employs elastomeric PDMS stamps to transfer micropatterns from masters patterned by conventional lithographic techniques to other substrates [37].

In the present study, CS/BSA micropatterns on functionalized Ti surfaces were prepared by $\mu\text{-TM}$. Alkali-treated Ti surfaces were first functionalized with 3-aminopropyltriethoxysilane (APTES), followed by glutaraldehyde (GA). Then, CS coatings were prepared on the Ti surfaces. Finally, BSA micropatterns were fabricated by $\mu\text{-TM}$. This study aims to explore the effect of continuously interconnected and discontinuous co-micropatterns on cell behavior. Two kinds of micropatterns were produced: microgrooves and microcylinders. The former represents a discontinuously grooved co-micropattern, with the rectangular CS region separated by BSA walls. The latter represents a continuously interconnected co-micropattern, with the net-like CS region separated by BSA cylinders. These CS/BSA co-micropatterns provided different chemical and physical cues for osteoblasts and could be used to study cell–cell interaction in the early culture stage.

2 Materials and methods

2.1 Titanium surface treatments

Before micropattern fabrication, Ti surfaces were treated as follows: alkali treatment, silanization, aldehydation, and final CS self-assembly. The whole process is schematically shown in Fig 1.

2.1.1 Alkali-treatment

Alkali treatment enriches OH groups on Ti surfaces to form a chemical bond with the silane coupling agent APTES [38]. Commercial pure titanium (CP-Ti) (Baoji Special Iron and Steel Co. Ltd., Shanxi, China) was cut into small plates with dimensions of 10 mm \times 10 mm \times 1 mm. The samples were mechanically polished by a series of 240, 400, 600, and 1,000 grit waterproof SiC paper. Subsequently, the samples were ultrasonically cleaned in acetone and deionized water, followed by alkali-treatment to form a Ti–OH layer on Ti surfaces. The alkali-treatment was adopted from the work of Kokubo et al. [39, 40]. NaOH solution (5 mol L⁻¹) was

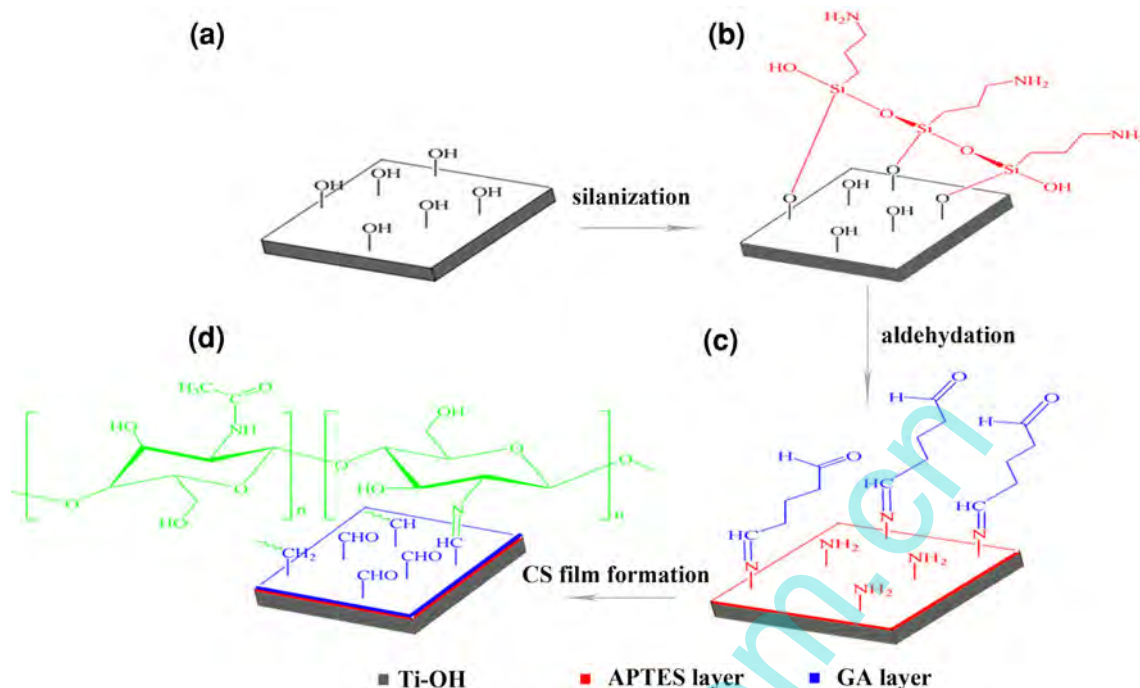


Fig. 1 Schematic drawing of four steps of Ti surface functionalization. **a** Alkali-treatment: a Ti-OH layer was formed on Ti surfaces; **b** Silanization: APTES $[(\text{CH}_3\text{CH}_2\text{O})_3\text{Si-NH}_2]$ bonded with Ti surfaces through Si-O-Ti bonds formed by a reaction between $\text{CH}_3\text{CH}_2\text{O}$ groups and OH on Ti surfaces. **c** Aldehydation: the one

aldehyde group of GA molecules directly reacted with NH_2 on the silanized surface to form imine bonds, leaving the other terminal $\text{C}=\text{O}$ available for developing imine bonds with CS molecules; and **d** CS film formation: CS films were linked to functionalized Ti surfaces by the reaction of NH_2 in CS and $\text{C}=\text{O}$ in GA to form Schiff bases

prepared by dissolving NaOH in ultrapure water. The cleaned Ti specimens were soaked in the alkaline solution at 60 °C for 3 h, washed with distilled water, and then dried at 40 °C for 24 h in an air atmosphere. The specimens after alkali-treatment were named as Ti-OH.

2.1.2 Silanization

In silanization, APTES $[(\text{CH}_3\text{CH}_2\text{O})_3\text{Si-NH}_2]$ bonded with Ti surfaces through Si-O-Ti bonds that were formed by a reaction between $\text{CH}_3\text{CH}_2\text{O}$ groups and OH on the Ti surfaces. The alkali-treated Ti specimens were soaked in the mixture (50 mL) of APTES (Sigma) and toluene (1 vol. %) at ambient temperature for 24 h. The adventitious moisture in the prepared mixture was absorbed by adding 5 g of anhydrous Na_2SO_4 . The specimens were ultrasonically cleaned thoroughly in toluene until the residues of physically adsorbed APTES were removed completely. The specimens were washed with ethanol followed by water and then further cured at 110 °C for 2 h to convert the hydrogen bonds between silane and Ti to covalent Si-O bonds [41].

2.1.3 Aldehydation

During aldehydation, the one aldehyde group of GA molecules directly reacted with NH_2 on the silanized surface to

form imine bonds, leaving the other terminal $\text{C}=\text{O}$ available for developing imine bonds with CS molecules. The specimens were immersed in 8 vol. % GA in deionized water at ambient temperature for 24 h, and then washed with deionized water to eliminate unbound GA. The specimens were then stored in a sealed petri dish.

2.1.4 Chitosan film formation

CS films were linked to functionalized Ti surfaces by the reaction of NH_2 in CS and $\text{C}=\text{O}$ in GA to form Schiff bases. CS powder was dissolved in 2 wt. % aqueous solution of glacial acetic acid, and the mixture was stirred to form a 1 wt. % light-yellow CS solution. The solution was cast onto silane-pretreated Ti specimens and then evaporated in a vacuum drier overnight at ambient temperature.

The elemental composition and chemical states of CP-Ti, Ti-OH, APTES-modified, GA-grafted, and CS-coated Ti surfaces were analyzed by an X-ray photoelectron spectrometer (XPS, PHI 5600, Physical Electronics, USA) equipped with a monochromatic aluminum $\text{K}\alpha$ source (1,486.71 eV of photons). Three samples for each treatment were probed, and the results were presented as the mean value. The surface morphology of the Ti specimens after the four aforementioned treatments and CS/BSA co-micropatterns were observed by an atomic force microscope (AFM, CSPM

5000, BenYuan, China) in contact mode. The roughness of root mean square (R_{rms}) was recorded, which was the average value of two parallel samples and five spots per sample based on a scan area of $25 \mu\text{m}^2$. After four treatments, the surfaces were also characterized by a Fourier transform-infrared (FT-IR) spectrometer (Nicolet 5700, Thermo Nicolet, USA).

2.2 Micropatterning

The BSA micropattern was prepared by μ -TM on the CS-coated Ti, and the process flow is shown in Fig. 2. First, a PDMS microstamp was fabricated by replicating the micropatterns of a micromachined silicon master produced by standard photolithography [42]. Briefly, Sylgard 184 (Dow Corning, USA) and initiator with a mass ratio of 10:1 were coated on the silicon master with micropatterns. The sample was then placed in a vacuum oven at 80°C for 2 h to exclude bubbles and to cure. Finally, the cured

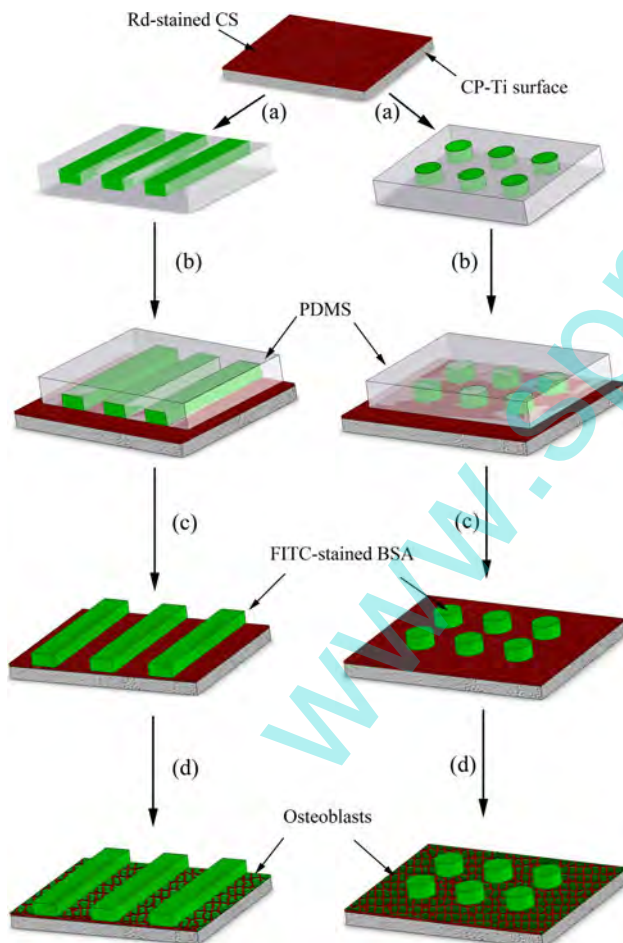


Fig. 2 Schematic drawing of the preparation of CS/BSA co-micropatterns by micro-transfer molding (μ -TM). **a** The BSA solution was dropped on the PDMS stamp; **b** the PDMS stamp with BSA was printed on CS-coated Ti surfaces; **c** the PDMS stamp was removed and **d** osteoblasts were seeded on microcylinders and microgrooves

polymer was striped off from the silicon master, and the PDMS stamp was obtained, which was the negative replica of the silicon master. The PDMS stamp was immersed in diluted hydrochloric acid for at least 12 h to increase surface hydrophilicity. Before patterning, the stamp was removed, rinsed with deionized water, and then dried.

Next, BSA (67 kDa, Shanghai Bio Life, China) was dissolved in a phosphate buffer solution to form the BSA solution with a concentration of 2 mg mL^{-1} . The buffer solution was prepared by dissolving NaH_2PO_4 (2.175 g), Na_2HPO_4 (3.375 g), and NaCl (2.125 g) in 500 mL of deionized water and buffered at pH 4.5 with 0.1 mol L^{-1} HCl. This pH is below the isoelectric point of BSA (5.0). Therefore, BSA can be positively charged when dissolved in phosphate-buffered saline (PBS). The BSA solution was dropped into the PDMS stamp, and the excess solution at bulgy regions of the PDMS stamp was scraped off. The PDMS stamp filled with the BSA solution was printed manually on the CS-coated Ti surface and then dried at 20°C for 2 h. Finally, the PDMS stamp was stripped off, and the BSA micropattern was obtained. Microgrooves with widths of 4 (G4), 24 (G24), and $38 \mu\text{m}$ (G38) and microcylinders with diameters of 10 (C10), 30 (C30), and $60 \mu\text{m}$ (C60) were prepared. Flat CS surfaces were also prepared to serve as the control.

BSA and CS were labeled with fluorescein isothiocyanate (FITC, Sigma-Aldrich, USA) and rhodamine 6G (Rd, Sigma-Aldrich, USA), respectively, to visualize the CS/BSA co-micropatterns on Ti surfaces. BSA and CS emitted green and red fluorescence, respectively. FITC-BSA powder was prepared by mixing FITC and the BSA solution (BSA:FITC = 50:1 mg). The mixture was stored in the dark for 12 h at 4°C , dialyzed to remove residual FITC, and then freeze-dried to obtain FITC-BSA powder. Rd-CS powder was prepared in the same way. The FITC-BSA/Rd-CS composite micropatterns were visualized under a fluorescence microscope (DMIL, Leica, Germany). The excitation wavelengths of FITC and Rd 6G were 488 and 543 nm, respectively. Three-dimensional (3D) images of the micropatterns were also visualized by AFM with a scan area of $100 \mu\text{m} \times 100 \mu\text{m}$ (CSPM 5000).

2.3 Cell culture

Bone marrow osteoblasts from male Sprague–Dawley rats were cultured to investigate their proliferation and morphology on pure CS and CS/BSA co-patterned Ti substrates. Before cell culture, the samples were sterilized under UV-light for 1.5 h in each side. The osteoblasts were cultured in α -Dulbecco's modified Eagle's medium containing 15 % fetal bovine serum at 37°C in a CO_2 atmosphere (5 %). The cell suspension (1 mL) was seeded on the specimen surface at a density of $1 \times 10^4 \text{ cells mL}^{-1}$. Afterward,

the samples were incubated for up to 7 days. The medium was replaced with fresh medium every 2 days. After incubation, the specimens were rinsed thrice with PBS (8.00 g L⁻¹ NaCl, 0.20 g L⁻¹ KCl, 2.90 g L⁻¹ Na₂HPO₄·12H₂O, and 0.20 g L⁻¹ KH₂PO₄). Then, the cells were fixed with 2.5 % GA, dehydrated, and then visualized under a scanning electron microscope (SEM; QUANTA-200, FEI, The Netherlands).

Cell proliferation was evaluated by the Alamar blue assay. This assay is based on the detection of cellular metabolic activity, which chemically reduces Alamar blue (BioSource, CA) and changes its color from blue to red. The assay was performed after 3 and 7 days of culture. During the Alamar blue assay, the culture medium in the 24-well plate was replaced with 300 μL of Medium 199 [without phenol red, with 10 % (v/v) serum and 10 % (v/v) Alamar blue]. The cells were incubated at standard cell culture conditions for 4 h. The optical absorbance of the medium was read at 600 and 570 nm against a medium-blank with Alamar blue on an enzyme-linked immunosorbent assay (ELISA) reader (MQX200, BioTEK, USA). The value of the difference (OD_{570 nm, cells} - OD_{600 nm, cells}) - (OD_{570 nm, blank} - OD_{600 nm, blank}) was recorded and used to calculate cell numbers. In each case, five specimens were tested, and the assay was repeated twice. The data were analyzed by one-way analysis of variance (ANOVA) followed by Tamhane’s T2 multiple-comparison post hoc test to determine the significance of difference between test groups. The level of statistical significance was set at *P* ≤ 0.05.

Osteoblast differentiation was measured by their alkaline phosphatase (ALP) activity, which was determined by monitoring the conversion of 4-nitrophenyl phosphate (4-NPP) to nitrophenol according to a previously described method [43, 44]. After 7 days of culture, the medium was removed from the wells, and the cell samples were washed twice with PBS. The cells were lysed using 300 μL well⁻¹ of 1 % Triton X-100 (Amresco, USA). The cell lysate was frozen and then thawed thrice to disrupt the cell membranes. The chromogenic substrate for ALP was 10 mmol L⁻¹ 4-NPP (Roche, Switzerland) dissolved in buffer solution (0.5 mol L⁻¹ Tris base and 2 mmol L⁻¹ MgCl₂·6H₂O). A 200 μL aliquot of the buffered substrate solution (10 mmol L⁻¹ 4-NPP) and a 50 μL aliquot of each cell lysate were added to a 96 96-well plate. The

concentration of ALP was determined by kinetic measurement of the absorbance at 405 nm in the ELISA reader using standards of defined ALP concentration.

3 Results and discussion

3.1 Ti functionization

The variation of atomic concentration from XPS analysis indicated successful silanization and aldehydation (Table 1). After APTES treatment, the concentrations of N and Si increased, and the atomic ratio of Si/N (1.15) was slightly higher than that of the APTES molecule (1.0). Iucci et al. explained the high atomic ratio of Si/N in terms of partial amine loss after polymerization [5]. After GA treatment, the concentrations of N and Si slightly decreased because GA did not contain N or Si. After CS treatment, the concentration of N further decreased because of the low quantity of amino groups in CS molecules.

High-resolution XPS spectra revealed the variation in the chemical state of elements after each treatment step, indicating treatment effectiveness. The high-resolution XPS spectra of O 1 s on CP-Ti and alkali-treated Ti were compared (Fig. 3). The results showed that alkali-treatment increased the concentration of OH on Ti surfaces. After alkali-treatment, the area ratio of deconvoluted OH sub-peak at 531.5 eV substantially increased from 18.2 to 32.2 % (Table 2). This relative OH concentration includes oxygen atoms in the most carbon compounds with C–O and O–C=O. Thus, the concentration of OH was corrected using the following formulas [45, 46].

First, the concentrations of C–O and O–C=O are calculated as

$$x(C - O) = \frac{I(C - O)}{I(C - H) + I(C - O) + I(O - C = O)} \quad (1)$$

$$x(O - C = O) = \frac{I(O - C = O)}{I(C - H) + I(C - O) + I(O - C = O)} \quad (2)$$

Substituting Eqs. (1) and (2) in Eq. (3), the concentration of OH is calculated as

Table 1 Atomic concentration (%) of Ti surfaces by XPS after various treatments

Samples	Carbon	Oxygen	Nitrogen	Silicon	Titanium
Ti	51.07 ± 6.46	32.94 ± 5.25	3.95 ± 0.95	0.58 ± 0.26	8.10 ± 2.93
Ti–OH	26.44 ± 1.27	46.13 ± 5.16	0.92 ± 0.02	0.40 ± 0.17	19.07 ± 0.74
APTES	55.51 ± 3.28	22.55 ± 1.39	9.56 ± 0.88	10.97 ± 0.96	0.36 ± 0.13
GA	61.78 ± 0.45	24.06 ± 0.64	6.32 ± 0.99	7.19 ± 0.29	0.21 ± 0.22
CS	67.94 ± 5.48	25.66 ± 4.52	5.10 ± 1.49	0.33 ± 0.36	0.01 ± 0.01

$$\begin{aligned}
 x(OH) &= \frac{I(OH)}{I(OH)_{measured} + I(TiO_2) + I(H_2O)} \times atom\%O \\
 &= \frac{[1 - x(C - O) \left(\frac{atom\%C}{atom\%O}\right) - x(O - C = O) \left(\frac{atom\%C}{atom\%O}\right)] \times I(OH)_{meas}}{I(OH)_{measured} + I(TiO_2) + I(H_2O)} \times atom\%O
 \end{aligned}
 \quad (3)$$

According to the aforementioned formulas, the concentration of OH on the alkali-treated Ti surfaces was 12.5 %, which was significantly larger than that on the bare Ti surface (3.4 %).

The high-resolution XPS spectra of C 1s after various treatments indicated the success of silanization and aldehydation (Fig. 4). The relative ratios of different peaks are listed in Table 3. The presence of carbon on the alkali-treated Ti surfaces (Fig. 4a) may be attributed to carbonaceous contamination. This finding was confirmed by spectral curve fitting with the peaks of C–C (285.0 eV), C–O (286.4 eV), and O–C=O (288.6 eV) [5]. After APTES treatment (Fig. 4b), the C 1s spectrum was curve fitted to three species. The peak at 285.0 eV was identified as C–C or C–H from the hydrocarbon chain of APTES and the

carbonaceous contamination. The peak at 286.4 eV was identified as the mixture of C–O or C–N [47]. The newly appeared peak at 284.0 eV with a relative area ratio of 34.2 % was identified as the C(SiO₃) of APTES [48, 49]. After GA treatment (Fig. 4c), two subpeaks at 287.3 and

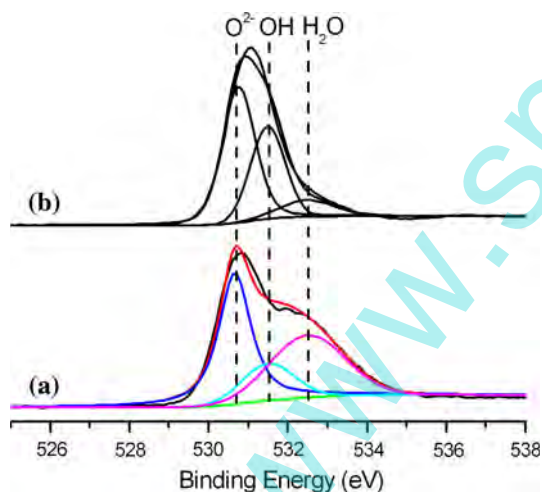


Fig. 3 Curve-fitted O 1s spectra of **a** CP-Ti surfaces and **b** Ti–OH surfaces after alkali treatment

Table 2 Peak species, binding energy and area ratio (%) of the high-resolution O 1s spectra on bare and alkali-treated Ti surfaces

Peak species	TiO ₂	OH	H ₂ O
(BE, eV)	530.0	531.5	532.5
Ti	41.2 ± 8.2	18.2 ± 3.5	40.7 ± 4.7
Ti–OH	51.6 ± 3.1	32.2 ± 2.3	16.2 ± 5.4

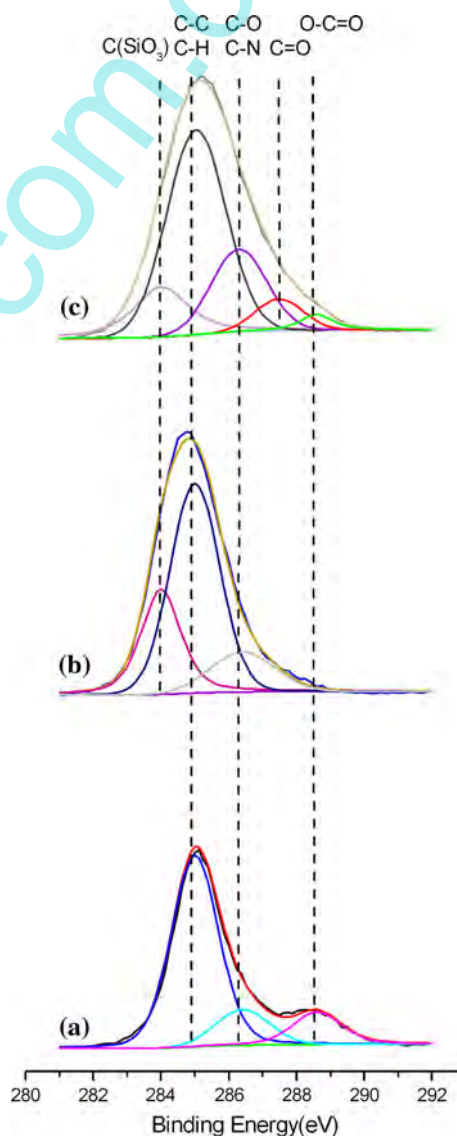


Fig. 4 Curve-fitted C 1s spectra of Ti surfaces after various treatments: **a** alkali treatment, **b** silanization with APTES, and **c** aldehydation with GA

Table 3 Peak species, binding energy and area ratio (%) of the high-resolution C 1 s spectra after various treatments

Peak Species	C(SiO ₃)	C–C, C–H	C–O, C–N	C=O	O–C=O
(BE, eV)	284.0	285.0	286.4	287.3	288.6
Ti	–	72.1 ± 4.3	15.4 ± 2.9	–	12.5 ± 1.9
Ti–OH	–	72.8 ± 4.7	16.8 ± 4.0	–	10.4 ± 3.1
APTES	34.2 ± 2.6	53.0 ± 3.5	12.9 ± 0.8	–	–
GA	13.7 ± 2.1	58.7 ± 7.3	19.1 ± 3.2	7.9 ± 4.2	2.5 ± 0.6

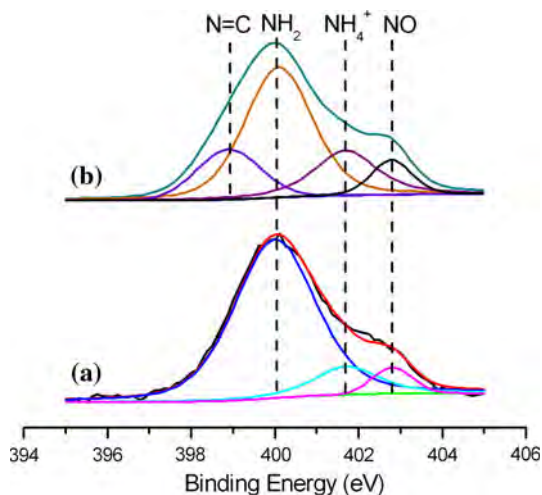


Fig. 5 Curve-fitted N 1 s spectra of Ti surfaces. **a** Silanization with APTES and **b** aldehydehydration with GA

Table 4 Peak species, binding energy and area ratio (%) of the high-resolution N 1 s spectra after silanization with APTES and aldehydehydration with GA

Peak Species	N=C	NH ₂	NH ₄ ⁺	NO
(BE, eV)	398.9	400.0	401.7	402.8
APTES	–	80.5 ± 1.5	18.1 ± 3.7	1.4 ± 2.9
GA	23.4 ± 6.9	51.6 ± 8.0	19.4 ± 6.4	5.6 ± 2.1

288.6 eV were observed, which were from C=O and/or C=N bondings (with an area ratio of 13.5 %) and the COOH groups in GA (with an area ratio of 4.5 %), respectively. The other two subpeaks (C–C/C–H, and C–O) showed a slight increase in area ratio. The former subpeak was ascribed to the five-carbon atom chain of GA. The latter subpeak was due to the polymeric structure formation of GA molecules under aqueous conditions, which was advantageous for the subsequent macromolecule coupling [50].

The high-resolution XPS spectra of N 1 s also exhibited significant changes after the different treatments (Fig. 5). The relative ratios of the different peaks are listed in Table 4. After APTES treatment (Fig. 5a), the peaks of N 1 s spectra were assigned as the primary amine groups

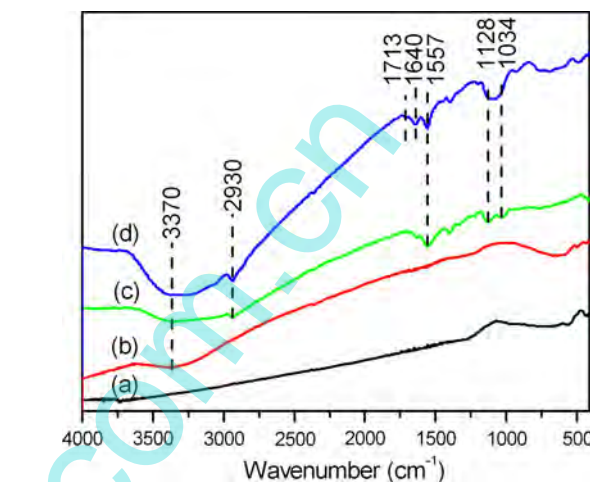


Fig. 6 FT-IR spectra of Ti surfaces after various treatments. **a** CP-Ti surface, **b** Ti–OH surfaces after alkali treatment, **c** silanization with APTES, and **d** aldehydehydration with GA

(NH₂ at 400 eV) of APTES [51], protonated amino groups (NH₄⁺ at 401.7 eV), and N–O (402.8 eV) [52]. After aldehydehydration (Fig. 5b), the peak area of the NH₂ groups significantly decreased because of the reaction of the aldehyde group of GA with the NH₂ group of APTES. A new subpeak of N=C appeared because of the aforementioned reaction between GA and APTES. The chemistry of GA after reacting with APTES remains controversial. For example, Martin et al. [53] did not find imine N in the N 1 s XPS spectrum of piranha-treated Ti modified with GA. They claimed the reaction between GA and APTES by the decrease of the intensity of C–N–H and NH₄⁺ subpeaks. Similarly, Minier et al. [51] did not discover imine N and only reported a weak C=N stretching vibration. Our results are in agreement with the reports of Longo [54]. In the study of Longo, imine N and a new subpeak (C=O) appeared in the N 1 s and C 1 s spectra, respectively. In C 1 s spectra, the ratio of C=N/C=O was higher than expected (1.0) because of the formation of GA oligomeric species. XPS data cannot be used to clarify the details of CS bonding with GA molecules because CS films are too thick to be penetrated by photoelectrons [55, 56].

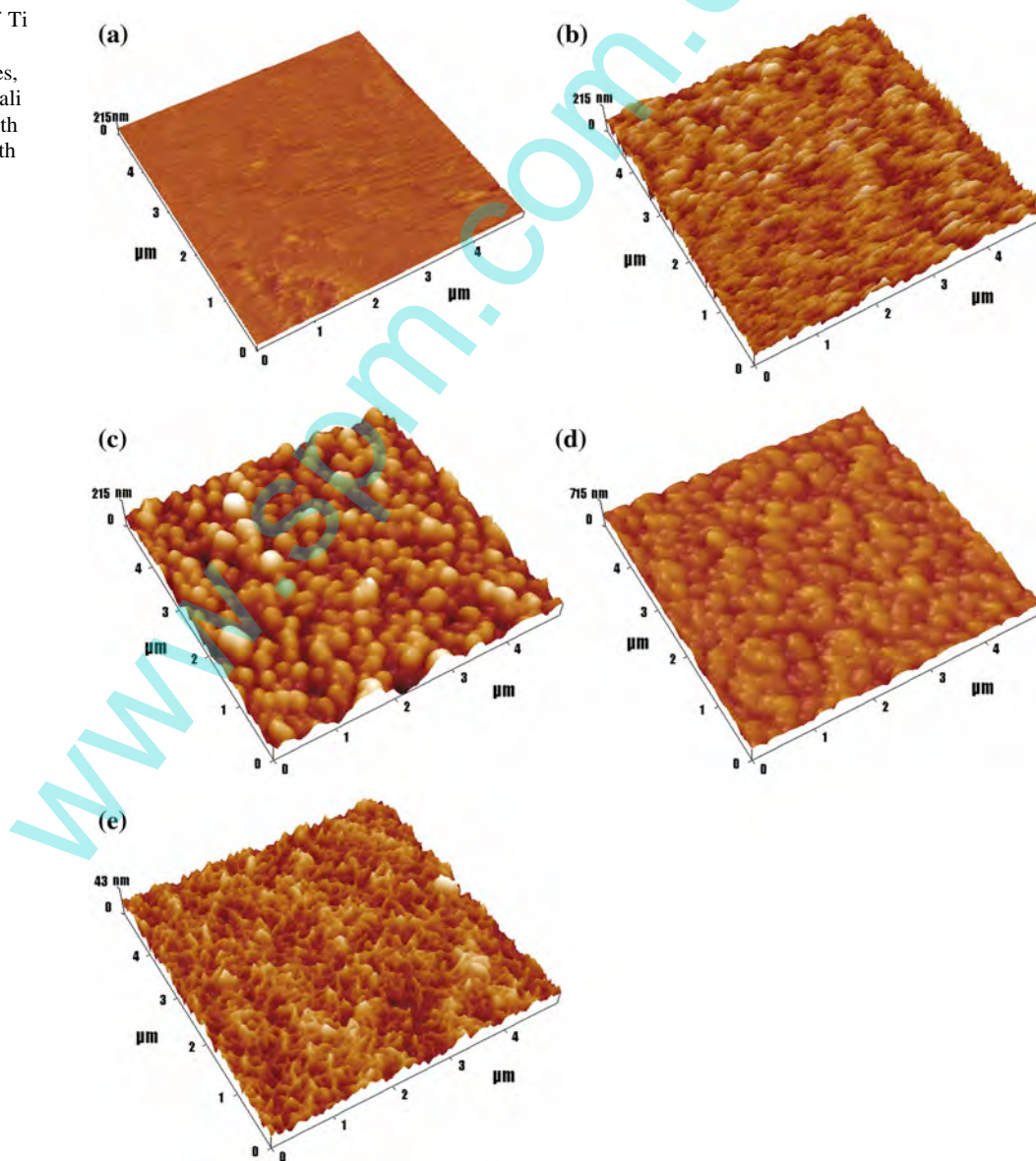
The treatments of Ti substrates were further investigated by FT-IR analysis (Fig. 6). Compared with CP-Ti

(Fig. 6a), a broad adsorption band around $3,370\text{ cm}^{-1}$ was found after alkali-treatment, indicating OH stretching vibrations (Fig. 6b). Figure 6c proves the introduction of APTES on the alkali-treated Ti surfaces. The characteristic adsorption band at $2,930\text{ cm}^{-1}$ was assigned to the alkyl C–H in APTES, and the vibration at $1,557\text{ cm}^{-1}$ was ascribed to the N–H bending mode of the NH_2 group. The absorption bands at $1,034$ and $1,128\text{ cm}^{-1}$ were assigned to Si–O moieties and the polymerization of certain Si–O moieties after curing, respectively [57]. After aldehydation (Fig. 6d), a slight but visible shoulder at $1,713\text{ cm}^{-1}$ and a new absorption band at $1,640\text{ cm}^{-1}$ were observed, representing contributions from the aldehyde group (C=O) of GA and imine group (C=N), respectively [58, 59]. The

FT-IR and XPS results suggested that GA bonded with APTES through C=N groups.

AFM images revealed the morphology of Ti substrates after the various treatments (Fig. 7). The Ti surface was smooth except for randomly distributed micro-fine scratches after mechanical grinding (Fig. 7a). The alkali-treated Ti surfaces presented a complex morphology of plate-like nanostructures perpendicular to the surface (Fig. 7b). Both APTES-treated (Fig. 7c) and GA-treated (Fig. 7d) surfaces exhibited globular-like nanostructures. The structures on the APTES-treated surfaces were smaller compared with those on the GA-treated surfaces. The CS-coated surfaces had nanoporous and nest-like structures (Fig. 7e). Table 5 lists the R_{rms} values of the

Fig. 7 3D AFM images of Ti surfaces after various treatments. **a** CP-Ti surfaces, **b** Ti–OH surfaces after alkali treatment, **c** silanization with APTES, **d** aldehydation with GA, and **e** CS-coated Ti surfaces



surfaces after the various treatments. The alkali-treated Ti surfaces were rougher than the mechanically polished surfaces. After silanization and aldehydation, the surface became even rougher. The CS-coated surface was the smoothest surface.

3.2 CS/BSA co-micropatterns

The fluorescent micrographs of co-patterned Rd-labeled CS and FITC-labeled BSA revealed well-defined green BSA micropatterns on red CS substrates (Fig. 8). The 3D images of

Table 5 Average roughness (R_{rms}) of Ti surfaces after various treatments

Samples	Ti	Ti-OH	APTES	GA	CS
R_{rms} (nm)	7.5 ± 3.2	17.8 ± 6.1	34.5 ± 10.6	47.2 ± 10.6	4.8 ± 1.4

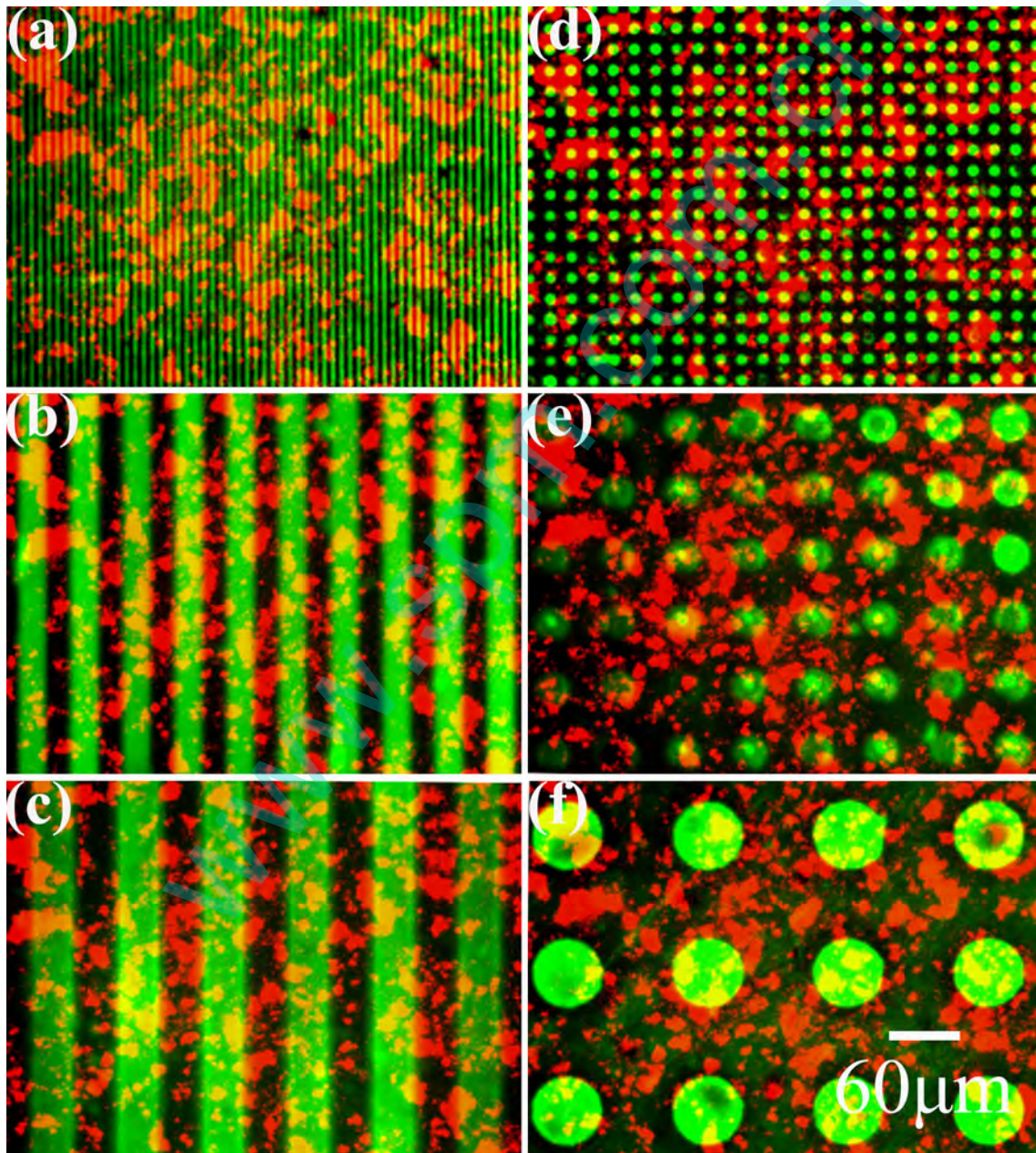


Fig. 8 Fluorescent micrographs of CS/BSA co-micropatterns on Ti surfaces: **a** G4, **b** G24, **c** G38, **d** C10, **e** C30, and **f** C60. The *green foreground* is FITC-labeled BSA, whereas the *red background* is Rd-labeled CS (Color figure online)

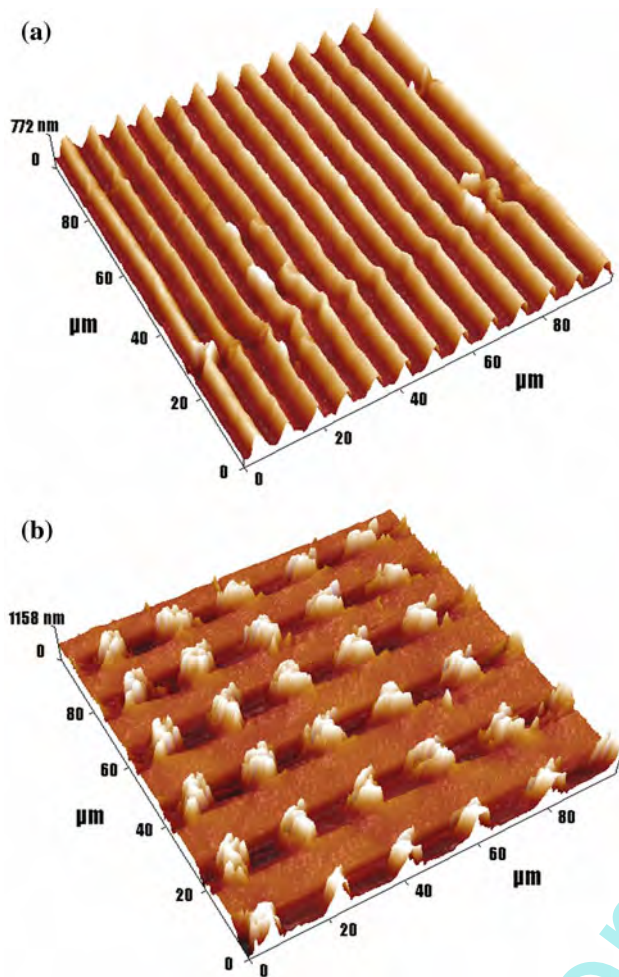


Fig. 9 Typical 3D AFM images of CS/BSA co-micropatterns: **a** G4 and **b** C10

CS/BSA co-micropatterns were also obtained by AFM (Fig. 9). The depths of G4, G24, and G38 were 410.0 ± 80.0 nm, $2,205.0 \pm 332.0$ nm, and $1,225.0 \pm 304.0$ nm, respectively. The heights of C10, C30, and C60 were 917.5 ± 60.1 nm, 983.8 ± 111.2 nm, and 606.0 ± 33.1 nm, respectively. The fluorescent and AFM micrographs demonstrated that the CS/BSA composite micropatterns were successfully produced on the Ti substrates by μ -TM.

3.3 Cell behavior

Osteoblasts showed different morphologies according to the different pattern features of CS/BSA. The SEM images of the cells cultured on the CS/BSA co-micropatterns with different sizes are shown in Fig. 10. After 7 days of culture, the cells on co-patterned microgrooves elongated within the CS regions, displaying a spindle-like morphology. The cells on microcylinders generally attached to the bottom of the CS regions because the positively charged CS molecules absorbed greater cell-adhesive proteins than

BSA molecules. In addition, the patterned BSA molecules excluded further attachment of extracellular matrix proteins and cells. Thus, the osteoblasts preferably attached to the CS regions. Although the BSA regions generally excluded osteoblast attachment, a few osteoblasts were still able to bridge BSA microgrooves and microcylinders when the micropattern size was in the same range as the cell diameter. In summary, the osteoblasts spread preferentially on the CS-rich regions and aligned with respect to the CS/BSA micropatterns. BSA did not completely repel the osteoblasts. They migrated to adjacent CS-rich regions. In the absence of any cues, the osteoblasts migrated randomly.

Alamar blue tests indicated that the shape rather than the size had a dominant effect on cell proliferation (Fig. 11). Microcylinders led to higher cell proliferation compared with microgrooves. After 3 and 7 days of culture, cell numbers on C10, C30, and C60 were all significantly higher compared with those on G4, G24, and G38 ($P < 0.05$). Comparison of cells on micropatterns with flat CS surfaces confirmed that the shape was an important factor affecting cell proliferation. Cell numbers on microgrooves were nearly the same as those on flat CS after 3 days of culture but were significantly smaller ($P < 0.05$) compared with those on flat CS after 7 days of culture. However, cell numbers on microcylinders were significantly larger than those on flat CS after 3 days of culture and were nearly the same as those on flat CS after 7 days of culture. These results suggested that cell–cell interaction at the initial culture stage was critical for cell proliferation because the cells in the bottom CS regions of microcylinders were interconnected but were separated in microgrooves. It was reported that endothelial cells and hepatocytes did not proliferate when they were cultured on the microscale islands that were separated by non-adhesive regions and therefore the culture lacked cell–cell contacts [33]. If pairs of such cells were placed on such islands, cell–cell contact increased and proliferation increased [60]. The results of the present study are consistent with these previous studies in terms of the importance of cell–cell interaction at the initial culture stage for cell proliferation. The results also suggest that cell proliferation can be regulated by the design of micropatterns.

The size of micropatterns also affected cell proliferation to a certain extent. Cell number on C10 was significantly higher than those on C30 and C60 after 3 and 7 days of culture because the diameter of C10 was small and the cells easily bridged the BSA regions. The effect of micropattern size was also reported in previous studies. Hasenbein et al. [61] reported that osteoblasts could attach to 50, 100, and 200 μ m circles modified with either arginine–glycine–aspartic acid–serine (RGDS) or lysine–arginine–serine–arginine (KRSR) micropatterns, but not to 10 μ m circular

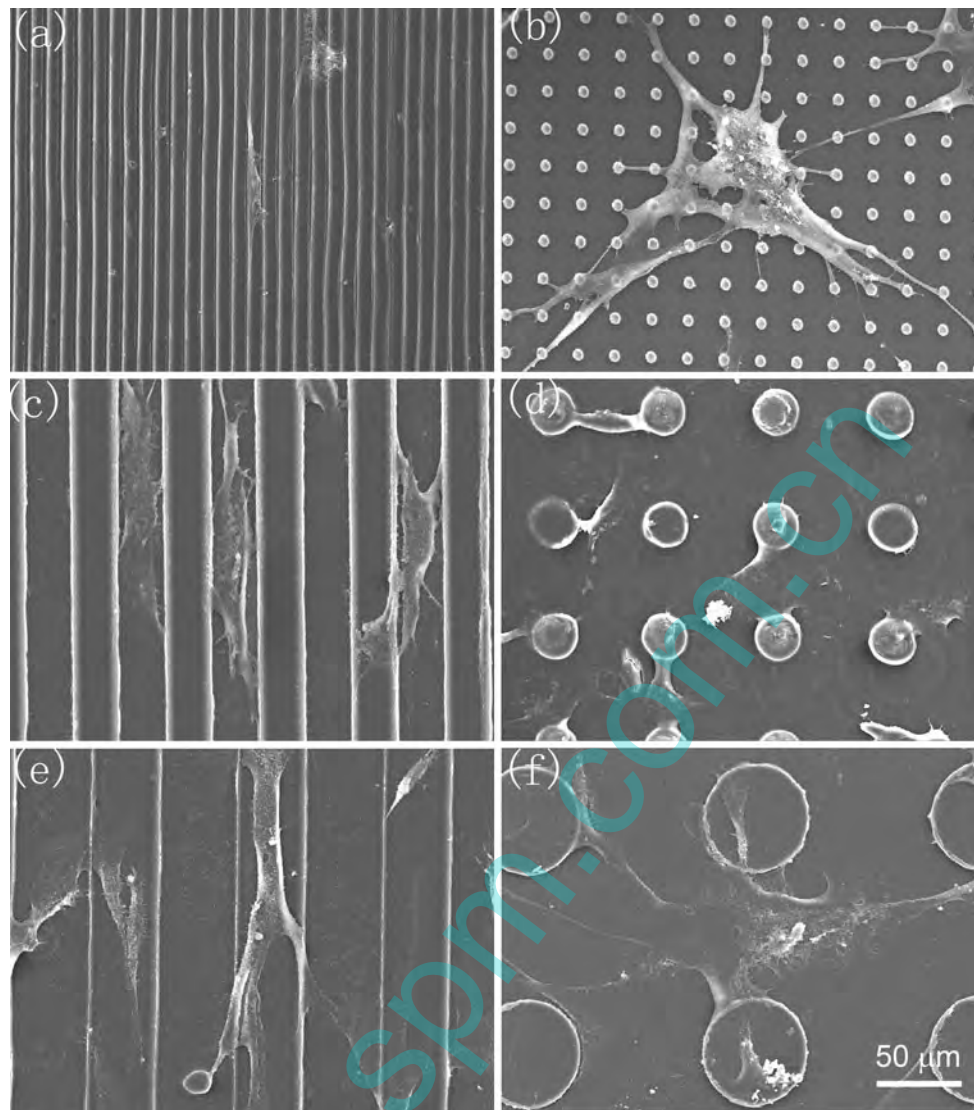


Fig. 10 Osteoblast morphology on micropatterns after 7 days of culture: **a** G4, **b** G24, **c** G38, **d** C10, **e** C30, and **f** C60

micropatterns smaller than the typical osteoblast size. Similarly, Chen et al. observed that bovine endothelial cells prefer attaching to 20, 30, and 40 μm square micropatterns rather than to 5 or 10 μm of the same pattern [62]. Wal-boomer et al. claimed that the cell size is approximately 20 μm ; therefore, micropatterns within 1 to 10 μm are optimum for cell alignment and proliferation [63]. In summary, the results of the present study further confirm that the micropattern size should not be greater than the actual cell size to allow cells to sense the topography of the surface.

The ALP assay indicated that cell differentiation was more sensitive to the size rather than to the shape of the micropatterns. Cell differentiation on discontinuous microgrooves was not significantly different from that on

continuously interconnected microcylinders. However, cell differentiation increased with increasing size of both micropatterns (Fig. 12). Although numerous factors could affect osteoblast differentiation, the change in cell shape caused by the microstructure of surfaces might be responsible for ALP production. Thomas et al. [64] reported that bone cells express osteocalcin mRNA when patterned on 400–10,000 μm^2 islands but not on flat control surfaces because micropatterns alter the shape of the nucleus of cells. Healy et al. [31] revealed a different rate of bone mineralization on striped EDS and OTS lanes. Those studies demonstrated that surface micropatterns mediate cell activity. In the present study, small micropatterns could limit cell differentiation, which may be ascribed to the severe cell shape change caused by small micropatterns.

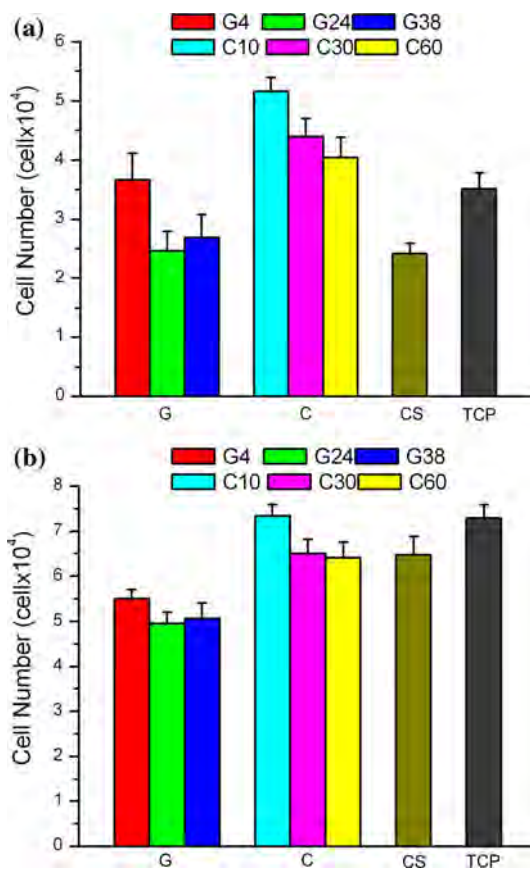


Fig. 11 Cell numbers on micropatterned surfaces after **a** 3 days and **b** 7 days of culture. CS represents flat CS coatings on Ti surfaces. TCP represents tissue culture plates

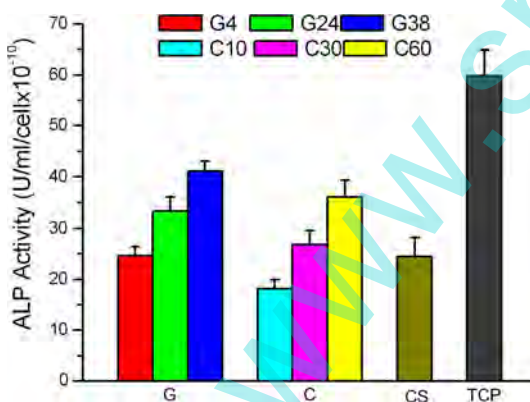


Fig. 12 ALP activity of cells on micropatterned surfaces after 7 days of culture

4 Conclusions

Micropatterns have become a powerful tool for investigating cell response to surface topography, which provide a possibility to mimic cell microenvironments and study cell function at the micrometer scale. This study investigates

the effects of the geometry and size of micropatterns on cell behavior using CS/BSA co-micropatterns on functionalized Ti surfaces. Microgrooves and microcylinders represent discontinuous and continuous micropatterns, respectively. The main findings are summarized as follows:

1. A comparison of cell behavior on continuous microcylinders and discontinuous microgrooves demonstrates that the shape rather than the size has a dominant effect on cell proliferation.
2. The size of micropatterns in the same range of cell diameters favors cell proliferation.
3. Cell differentiation is more sensitive to the size rather than to the shape of micropatterns.

Cell behavior can be regulated by the design of micropatterns with different types of materials, which is a new approach of studying the interaction between micropatterns and cells. This study demonstrates that cell behavior is different on microgrooves and microcylinders. The findings provide new insights into the mechanism of cell response to the microgeometry of biomaterial surfaces and present general implications on the microgeometrical design of biomaterial surfaces.

Acknowledgments This project was financially supported by the National Basic Research Program of China (973 Program, 2012CB933602), NSFC (31070851), Program for New Century Excellent Talents in University (NCET-10-0704), Sichuan Youth Science-Technology Foundation (2011JQ0010), Fundamental Research Funds for the Central Universities (SWJTU11CX150).

References

1. Liu XY, Chu PK, Ding CX. Surface modification of titanium, titanium alloys, and related materials for biomedical applications. *Mat Sci Eng R*. 2004;47:49–121.
2. Lu X, Leng Y, Zhang X, Xu J, Qin L, Chan C. Comparative study of osteoconduction on micromachined and alkali-treated titanium alloy surfaces in vitro and in vivo. *Biomaterials*. 2005;26:1793–801.
3. Dettin M, Herath T, Gambaretto R, Iucci G, Battocchio C, Bagno A, et al. Assessment of novel chemical strategies for covalent attachment of adhesive peptides to rough titanium surfaces: XPS analysis and biological evaluation. *J Biomed Mater Res A*. 2009; 91A:463–79.
4. Secchi AG, Grigoriou V, Shapiro IM, Cavalcanti-Adam EA, Composto RJ, Ducheyne P, et al. RGDS peptides immobilized on titanium alloy stimulate bone cell attachment, differentiation and confer resistance to apoptosis. *J Biomed Mater Res A*. 2007; 83A:577–84.
5. Iucci G, Dettin M, Battocchio C, Gambaretto R, Bello CD, Polzonetti G. Novel immobilizations of an adhesion peptide on the TiO₂ surface: an XPS investigation. *Mat Sci Eng C-Bio S*. 2007;27:1201–6.
6. Maekawa K, Yoshida Y, Mine A, Fujisawa T, Meerbeek BV, Suzuki K, et al. Chemical interaction of polyphosphoric acid with titanium and its effect on human bone marrow derived mesenchymal stem cell behavior. *J Biomed Mater Res A*. 2007;82A:195–200.

7. Maekawa K, Yoshida Y, Mine A, Meerbeek BV, Suzuki K, Kuboki T. Effect of polyphosphoric acid pre-treatment of titanium on attachment, proliferation, and differentiation of osteoblast-like cells (MC3T3-E1). *Clin Oral Implants Res.* 2008;19:320–5.
8. Rammelt S, Schulze E, Bernhardt R, Hanisch U, Scharnweber D, Worch H, et al. Coating of titanium implants with type-I collagen. *J Orthop Res.* 2004;22:1025–34.
9. Yang Y, Cavin R, Ong JL. Protein adsorption on titanium surfaces and their effect on osteoblast attachment. *J Biomed Mater Res A.* 2003;67A:344–9.
10. Liu H, Du Y, Yang J, Zhu H. Structural characterization and antimicrobial activity of chitosan/betaine derivative complex. *Carbohydr Polym.* 2004;55:291–7.
11. Arpornmaeklong P, Pripatnanont P, Suwatwirote N. Properties of chitosan-collagen sponges and osteogenic differentiation of rat-bone-marrow stromal cells. *Int J Oral Max Surg.* 2008;37:357–66.
12. Bumgardner JD, Wiser R, Gerard PD, Bergin P, Chestnutt B, Marini M, et al. Chitosan: potential use as a bioactive coating for orthopaedic and craniofacial/dental implants. *J Biomater Sci Polym E.* 2003;14:423–38.
13. Bumgardner JD, Chesnutt BM, Yuan Y, Yang Y, Appleford M, Oh S, et al. The integration of chitosan-coated titanium in bone: an in vivo study in rabbits. *Implant Dent.* 2007;16:66–79.
14. Kaji H, Kanada M, Oyamatsu D, Matsue T, Nishizawa M. Microelectrochemical approach to induce local cell adhesion and growth on substrates. *Langmuir.* 2003;20:16–9.
15. Kaji H, Tsukidate K, Hashimoto M, Matsue T, Nishizawa M. Patterning the surface cytophobicity of an albumin-physisorbed substrate by electrochemical Means. *Langmuir.* 2005;21:6966–9.
16. den Braber ET, Jansen HV, de Boer MJ, Croes HJE, Elwenspoek M, Ginsel LA, et al. Scanning electron microscopic, transmission electron microscopic, and confocal laser scanning microscopic observation of fibroblasts cultured on microgrooved surfaces of bulk titanium substrata. *J Biomed Mater Res A.* 1998;40:425–33.
17. Qu J, Chehroudi B, Brunette D. The use of micromachined surfaces to investigate the cell behavioural factors essential to osseointegration. *Oral Dis.* 1996;2:102–15.
18. Hamilton DW, Wong KS, Brunette DM. Microfabricated discontinuous-edge surface topographies influence osteoblast adhesion, migration, cytoskeletal organization, and proliferation and enhance matrix and mineral deposition in vitro. *Calcif Tissue Int.* 2006;78:314–25.
19. Zinger O, Zhao G, Schwartz Z, Simpson J, Wieland M, Landolt D, et al. Differential regulation of osteoblasts by substrate microstructural features. *Biomaterials.* 2005;26:1837–47.
20. Mata A, Boehm C, Fleischman AJ, Muschler G, Roy S. Growth of connective tissue progenitor cells on microtextured polydimethylsiloxane surfaces. *J Biomed Mater Res A.* 2002;62:499–506.
21. Ito Y. Micropattern immobilization of polysaccharide. *J Inorg Biochem.* 2000;79:77–81.
22. Heydari M, Hasuda H, Sakuragi M, Yoshida Y, Suzuki K, Ito Y. Modification of the titan surface with photoreactive gelatin to regulate cell attachment. *J Biomed Mater Res A.* 2007;83A:906–14.
23. Gopalan SM, Flaim C, Bhatia SN, Hoshijima M, Knoell R, Chien KR, et al. Anisotropic stretch-induced hypertrophy in neonatal ventricular myocytes micropatterned on deformable elastomers. *Biotechnol Bioeng.* 2003;81:578–87.
24. Hsu SH, Su CH, Chiu IM. A novel approach to align adult neural stem cells on micropatterned conduits for peripheral nerve regeneration: a feasibility study. *Artif Organs.* 2009;33:26–35.
25. Hsu SH, Chen CY, Lu PS, Lai CS, Chen CJ. Oriented Schwann cell growth on microgrooved surfaces. *Biotechnol Bioeng.* 2005;92:579–88.
26. Moroni L, Lee LP. Micropatterned hot-embossed polymeric surfaces influence cell proliferation and alignment. *J Biomed Mater Res A.* 2009;88A:644–53.
27. Karp JM, Yeo Y, Geng W, Cannizarro C, Yan K, Kohane DS, et al. A photolithographic method to create cellular micropatterns. *Biomaterials.* 2006;27:4755–64.
28. Yamazoe H, Okuyama T, Suzuki H, Fukuda J. Fabrication of patterned cell co-cultures on albumin-based substrate: applications for microfluidic devices. *Acta Biomater.* 2010;6:526–33.
29. Lu X, Leng Y. Comparison of the osteoblast and myoblast behavior on hydroxyapatite microgrooves. *J Biomed Mater Res B Appl Biomater.* 2009;90B:438–45.
30. Lu X, Leng Y. Quantitative analysis of osteoblast behavior on microgrooved hydroxyapatite and titanium substrata. *J Biomed Mater Res A.* 2003;66A:677–87.
31. Healy KE, Thomas CH, Rezanian A, Kim JE, McKeown PJ, Lom B, et al. Kinetics of bone cell organization and mineralization on materials with patterned surface chemistry. *Biomaterials.* 1996;17:195–208.
32. Kam L, Shain W, Turner JN, Bizios R. Correlation of astroglial cell function on micro-patterned surfaces with specific geometric parameters. *Biomaterials.* 1999;20:2343–50.
33. Singhvi R, Kumar A, Lopez G, Stephanopoulos G, Wang D, Whitesides G, et al. Engineering cell shape and function. *Science.* 1994;264:696–8.
34. Clark P, Connolly P, Moores G. Cell guidance by micropatterned adhesiveness in vitro. *J Cell Sci.* 1992;103:287–92.
35. Feng J, Gao C, Wang B, Shen J. Co-patterning chitosan and bovine serum albumin on an aldehyde-enriched glass substrate by microcontact printing. *Thin Solid Films.* 2004;460:286–90.
36. Xie J, Lu X, Zhang H, Zhou X, Qu S, Feng B, et al. Preparation and characterization of the CS/BSA composite micropatterns on silicon surfaces. *Chem J Chin Univ.* 2009;30:2319–25.
37. Xia Y, Whitesides GM. *Soft lithogr Annu Rev Mater Sci.* 1998;28:153–84.
38. Kang HJ, Blum FD. Structure and dynamics of amino functional silanes adsorbed on silica surfaces. *J Phys Chem A.* 2002;95:9391–6.
39. Kokubo T, Miyaji F, Kim HM, Nakamura T. Spontaneous formation of bone like apatite layer on chemically treated titanium metals. *J Am Ceram Soc.* 1996;79:1127–9.
40. Kim HM, Miyaji F, Kokubo T, Nakamura T. Preparation of bioactive Ti and its alloys via simple chemical surface treatment. *J Biomed Mater Res.* 1996;32:409–17.
41. Bumgardner JD, Wiser R, Patrick DG, Bergin P, Chestnutt B, Marini M, et al. Chitosan: potential use as a bioactive coating for orthopaedic and craniofacial/dental implants. *J Biomater Sci Polym E.* 2003;14:423–38.
42. Jiang L, Lu X, Leng Y, Qu S, Feng B, Weng J. Micropatterned TiO₂ effects on calcium phosphate mineralization. *Mat Sci Eng C Bio S.* 2009;29:2355–9.
43. Sabokbar A, Millett PJ, Myer B, Rushton N. A rapid, quantitative assay for measuring alkaline phosphatase activity in osteoblastic cells in vitro. *Bone Mineral.* 1994;27:57–67.
44. Liu YR, Qu SX, Maitz MF, Tan R, Weng J. The effect of the major components of *Salvia Miltiorrhiza* Bunge on bone marrow cells. *J Ethnopharmacol.* 2007;111:573–83.
45. McCafferty E, Wightman JP, Cromer TF. Surface properties of hydroxyl groups in the air-formed oxide film on titanium. *J Electrochem Soc.* 1999;146:2849–52.
46. McCafferty E, Wightman JP. Determination of the concentration of surface hydroxyl groups on metal oxide films by a quantitative XPS method. *Surf Interface Anal.* 1998;26:549–64.
47. Szili EJ, Kumar S, Smart RSC, Voelcker NH. Generation of a stable surface concentration of amino groups on silica coated onto titanium substrates by the plasma enhanced chemical vapour deposition method. *Appl Surf Sci.* 2009;255:6846–50.
48. Porté-Durrieu MC, Labrugère C, Villars F, Lefebvre F, Dutoya S, Guette A, et al. Development of RGD peptides grafted onto silica

- surfaces: XPS characterization and human endothelial cell interactions. *J Biomed Mater Res A*. 1999;46:368–75.
49. Laffon C, Flank A, Lagarde P, Laridjani M, Hagege R, Olry P, et al. Study of Nicalon-based ceramic fibres and powders by EXAFS spectrometry, X-ray diffractometry and some additional methods. *J Mater Sci*. 1989;24:1503–12.
 50. Walt DR, Agayn VI. The chemistry of enzyme and protein immobilization with glutaraldehyde. *Trends Anal Chem*. 1994;13:425–30.
 51. Minier M, Salmain M, Yacoubi N, Barbes L, Méthivier C, Zanna S, et al. Covalent immobilization of lysozyme on stainless steel interface spectroscopic characterization and measurement of enzymatic activity. *Langmuir*. 2005;21:5957–65.
 52. Pashutski A, Folman M. Low temperature XPS studies of NO and N₂O adsorption on Al(100). *Surf Sci*. 1989;216:395–408.
 53. Martin HJ, Schulz KH, Bumgardner JD, Walters KB. XPS study on the use of 3-aminopropyltriethoxysilane to bond chitosan to a titanium surface. *Langmuir*. 2007;23:6645–51.
 54. Longo L, Vasapollo G, Guascito M, Malitesta C. New insights from X-ray photoelectron spectroscopy into the chemistry of covalent enzyme immobilization, with glutamate dehydrogenase (GDH) on silicon dioxide as an example. *Anal Bioanal Chem*. 2006;385:146–52.
 55. Moulder JF, Stickle WF, Sobel PE, Bomben KD. *Handbook of X-ray photoelectron spectroscopy*. Ramsey: Perkin-Elmer Corporation; 1992.
 56. Martin HJ, Schulz KH, Bumgardner JD, Schneider JA. Enhanced bonding of chitosan to implant quality titanium via four treatment combinations. *Thin Solid Films*. 2008;516:6277–86.
 57. Kim J, Seidler P, Fill C, Wan LS. Investigations of the effect of curing conditions on the structure and stability of amino-functionalized organic films on silicon substrates by Fourier transform infrared spectroscopy, ellipsometry, and fluorescence microscopy. *Surf Sci*. 2008;602:3323–30.
 58. Yang G, Wu J, Xu G, Yang L. Comparative study of properties of immobilized lipase onto glutaraldehyde-activated amino-silica gel via different methods. *Colloid Surf B*. 2010;78:351–6.
 59. Monteiro OA, Airoidi C. Some studies of crosslinking chitosan-glutaraldehyde interaction in a homogeneous system. *Int J Biol Macromol*. 1999;26:119–28.
 60. Nelson CM, Chen CS. Cell-cell signaling by direct contact increases cell proliferation via a PI3K-dependent signal. *FEBS Lett*. 2002;514:238–42.
 61. Hasenbein ME, Andersen TT, Bizios R. Micropatterned surfaces modified with select peptides promote exclusive interactions with osteoblasts. *Biomaterials*. 2002;23:3937–42.
 62. Chen CS, Mrksich M, Huang S, Whitesides GM, Ingber DE. Micropatterned surfaces for control of cell shape, position, and function. *Biotechnol Prog*. 1998;14:356–63.
 63. Walboomers XF, Croes HJE, Ginsel LA, Jansen JA. Growth behavior of fibroblasts on microgrooved polystyrene. *Biomaterials*. 1998;19:1861–8.
 64. Thomas CH, Collier JH, Sfeir CS, Healy KE. Engineering gene expression and protein synthesis by modulation of nuclear shape. *Proc Natl Acad Sci USA*. 2002;99:1972–7.